energy&fuels

pubs.acs.org/EF

Article

Enhancing Ni Exsolution by Nonmetal B-Site Substituents (Si and P) in $SrTiO_3$-Based Solid Oxide Fuel Cell Anodes

Md Raziun Bin Mamtaz, Zheng Wang, Alessio Belotti, Emanuele Quattrocchi, Jing Yu, Jiapeng Liu, and Francesco Ciucci*

Cite This: https://doi.org/10.1021/acs.energyfuels.1c01985

Read Online

ACCESS | Metrics & More | Article Recommendations | Supporting Information

ABSTRACT: In situ nanoparticle exsolution is an excellent strategy to enhance the electrocatalytic activity of solid oxide fuel cell (SOFC) electrodes. Herein, we report that Si and P can be used as B-site nonmetal substituents to improve the electrochemical performance of the model SOFC anode $SrTiO_{3-\delta}$ after testing different Si- and P-substitution levels. First-principles calculations show that Si- or P-substitution promotes the Ni diffusion as well as its segregation toward the surface. Related experiments show that the area-specific resistance (ASR) measured at 800 °C in 3% humidified H_2 improves upon Si- and P-substitution from 0.600 Ω cm^2 for $Sr_{0.8}Ti_{0.9}Ni_{0.1}O_{3-\delta}$ (STN) to 0.061 Ω cm^2 for $Sr_{0.8}Ti_{0.85}Ni_{0.1}Si_{0.05}O_{3-\delta}$ and 0.056 Ω cm^2 for $Sr_{0.8}Ti_{0.85}Ni_{0.1}P_{0.05}O_{3-\delta}$. Moreover, the P-substituted material shows excellent stability with a symmetric cell, retaining its ASR for 70 h in 3% humidified H_2. X-ray photoelectron spectroscopy measurements reveal that even a slight nonmetal substitution can reduce Ni to a lower oxidation state than STN before exsolution. In turn, this promotes the reduction of Ni during exsolution, which improves the ASR. For the first time, nonmetal substituents in perovskite oxides are utilized to aid Ni exsolution from the host lattice, opening new avenues to improve the electrochemical activity.

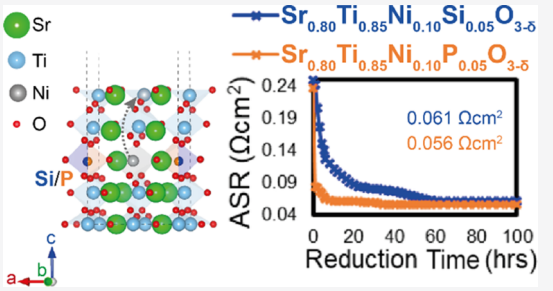

1. INTRODUCTION

Solid oxide fuel cells (SOFCs) and solid oxide electrolysis cells are highly efficient (>60%) and fuel-flexible systems capable of operating with H_2, C_2H_5OH, CH_4, CO, and so forth.[1] In light of these beneficial properties, these broad solid oxide cell (SOC) technologies have the potential to alleviate the impact of fossil fuels on the environment.[2] However, their high operating temperature (600−1000 °C) has drawbacks, such as (i) low durability due to fast electrochemical degradation and mechanical instabilities [because of thermal expansion coefficient (TEC) mismatch between electrode and electrolyte materials]; (ii) the need for complex thermal management systems; and (iii) the high cost of materials for sealings and interconnects.[3,4]

To realize fuel flexibility, the anode is a crucial component for which stable and electrochemically active materials are needed.[3] Several factors are critically important to the anode performance, including good electrical conductivity, thermal expansion compatibility with the electrolyte, sufficient porosity, and more importantly high electrochemical activity.[2,5−8] To increase the activity, we can resort to impregnating the anode with nanoparticles as transition-metal nanoparticles can be highly active catalysts for fuel oxidation reactions.[5−7] However, these nanoparticles are just deposited on the surface of anode materials, binding weakly to them and agglomerating easily during SOC operation. Additionally, deposited nanoparticles can be easily poisoned by hydrocarbon fuels.[9,10] These impediments result in severe performance degradation. Therefore, it is imperative to ameliorate transition-metal nanoparticles' stability. Strongly anchored and well-distributed nanoparticles can be generated by the exsolution process from ABO_3 perovskite oxides.[5,10,14] The engrained nanoparticles produced from exsolution do not migrate over the surfaces or lift-off when exposed to CH_4.[5,6,10] Typically, if an $AB_{1-x}B'_xO_{3-\delta}$ perovskite oxide is subjected to a reducing environment, then the more easily reducible cation B′ diffuses through the bulk host lattice, nucleates, and finally egresses from the surface as a metal nanoparticle.[5,11−14]

Nishihata et al. were the first to produce exsolved nanoparticles by egressing Pd from $LaFe_{0.57}Co_{0.38}Pd_{0.05}O_3$.[11] A decade later,[13] in a breakthrough article,[14] Irvine's group demonstrated that A-site deficiency $A_{1-x}B_{1-x}B'_xO_{3-\delta}$ produces a greater yield of exsolved B′, promoting the exsolution of B′s which are not easily reduced, such as Fe (see Note S1).[14−16] For SOFC's hydrogen oxidation reaction, Ni has been identified as an effective electrocatalyst.[8,17] Consequently, exsolution of Ni has been carried out in a range of perovskite

Received: June 18, 2021
Revised: August 18, 2021

Table 1. Different Compositions of Materials Synthesized and Named as "STXN(S/P)Y" Where *X* Refers to the Ti Stoichiometric Amount and *Y* Refers to the Si/P Stoichiometric Amount in $Sr_{0.8}Ti_XNi_{0.1}(Si/P)_YO_{3-\delta}$, as Other Elements' Stoichiometry Remains Unchanged[a]

material	name	structure	nonmetal amount [%]	A-site deficiency [%]
$Sr_{0.8}Ti_{0.9}Ni_{0.1}O_{3-\delta}$	ST90N	*I*4/*mcm*	0	20
$Sr_{0.8}Ti_{0.85}Ni_{0.1}Si_{0.05}O_{3-\delta}$	ST85NS5	*I*4/*mcm*	5	20
$Sr_{0.8}Ti_{0.8}Ni_{0.1}Si_{0.1}O_{3-\delta}$	ST80NS10	*I*4/*mcm*	10	20
$Sr_{0.8}Ti_{0.9}Ni_{0.1}Si_{0.05}O_{3-\delta}$	ST90NS5	*I*4/*mcm*	5	24
$Sr_{0.8}Ti_{0.85}Ni_{0.1}P_{0.05}O_{3-\delta}$	ST85NP5	*I*4/*mcm*	5	20
$Sr_{0.8}Ti_{0.8}Ni_{0.1}P_{0.1}O_{3-\delta}$	ST80NP10	*I*4/*mcm*	10	20
$Sr_{0.8}Ti_{0.9}Ni_{0.1}P_{0.05}O_{3-\delta}$	ST90NP5	*I*4/*mcm*	5	24

[a]The "nonmetal amount" column refers to the substitution of Ti by a nonmetal and "A-site deficiency" column refers to the variation from 1:1 A-site to B-site ratio in perovskite oxide.

oxides, including $La_{0.4}Sr_{0.4}Sc_{0.9}Ni_{0.1}O_{3-\delta}$,[5] $La_xSr_{0.8-x}Ti_{1-y}Ni_yO_{3-\delta}$,[10,16] and $(Sr_{0.94})_{0.9}(Ti_{0.9}Nb_{0.1})_{0.9}Ni_{0.1}O_3$.[18]

$SrTiO_3$ (STO) is considered as a model SOFC anode material[10,14] because of its thermochemical stability under reducing conditions due to the strong Ti−O bonds.[19] Nevertheless, STO is a poor oxygen and electron conductor with an electronic conductivity in the order of 10^{-2} to 10^{-4} S cm^{-1} at 1000 °C.[19] La in the A-site has been used to enhance STO's electrical conductivity to 0.01−500 S cm^{-1} at 800−1000 °C.[14,16,20] However, Gao et al.[16] reported that La-doping hinders Ni diffusion which consequently limits Ni exsolution.[10,16] In the same study,[16] the area-specific resistance (ASR) decrement was employed as an indicator of the Ni exsolution rate because as more Ni nanoparticles appear, the catalytic activity increases, lowering the ASR. Therein, the ASR of Ni-doped STO improved greatly from 0.60 to 0.05 Ω cm^2 at 800 °C in 3% humidified H_2 through La-substitution.[16] Gao et al. associated this improvement with the higher electrical conductivity.[16]

Hancock et al. showed that for $SrCoO_3$ and $SrMnO_3$ perovskites, doping nonmetals (such as Si and P) in the B-site leads to the reduction of the parent B-site transition metals (Co and Mn) and an increased oxygen deficiency.[21−23] In addition, electrical conductivity improved by 1−2 orders of magnitude by introducing Si[22] and P.[21] Furthermore, Si and P were also utilized to stabilize the cubic phases of Sr(Co/Mn)O_3.[21−23] Herein, Ni exsolution in Si- or P-substituted STO is studied, with Si and P entering the B-site as SiO_4^{4-} and PO_4^{3-} which replace TiO_6^{8-} and aid the oxygen vacancy formation, see Figure S1a.[21−23] The resulting oxygen vacancies promote the reduction of Ni and, in turn, Ni exsolution.[10,14,16] In addition, Si^{4+} (0.260 Å) and P^{5+} (0.170 Å) have smaller ionic radii than Ti^{4+} (0.605 Å) and Ni^{2+} (0.690 Å),[24] implying that the Si−O and P−O bonds are shorter than Ti−O and Ni−O bonds. As illustrated in Figure S1b, this bond length difference can cause distortion in the host lattice. Since Ni−O bonds are weaker than Ti−O,[14,16] Ni−O lengthens and weakens, thereby enhancing Ni migration. Moreover, the Ni''_{Ti}, $Si^{\times}_{Ti}$, and $P^{\bullet}_{Ti}$ defects (denoted with Kröger−Vink notations) can influence the Ni segregation.

We used density functional theory (DFT) calculations to assess how Si and P influence Ni exsolution. We first computed the Ni segregation energetics of slab models derived from STO. Then, using the climbing image nudged elastic band (CINEB) method, we investigated the impact of Si-/P-substitution on the Ni transportation barrier. In parallel, oxygen vacancy formation energies and density of states (DOS) were computed. To validate the computational findings, we synthesized the following materials: $Sr_{0.8}Ti_{0.85}Ni_{0.1}Si_{0.05}O_{3-\delta}$ (ST85NS5), $Sr_{0.8}Ti_{0.8}Ni_{0.1}Si_{0.1}O_{3-\delta}$ (ST80NS10), $Sr_{0.8}Ti_{0.9}Ni_{0.1}Si_{0.05}O_{3-\delta}$ (ST90NS5), $Sr_{0.8}Ti_{0.85}Ni_{0.1}P_{0.05}O_{3-\delta}$ (ST85NP5), $Sr_{0.8}Ti_{0.8}Ni_{0.1}P_{0.1}O_{3-\delta}$ (ST80NP10), and $Sr_{0.8}Ti_{0.9}Ni_{0.1}P_{0.05}O_{3-\delta}$ (ST90NP5), which we compared against $Sr_{0.8}Ti_{0.9}Ni_{0.1}O_{3-\delta}$ (ST90N) (Table 1). The compounds were characterized structurally and electrochemically, and the compositions with higher activity were further analyzed for thermochemical stability and electrochemical performance.

Our combined experimental/computational efforts suggest the following: (i) Ni exsolution and diffusion benefit from the presence of Si and P as B-site substitutional defects and (ii) 5% substituted samples (ST85NS5 and ST85NP5) are the best among the materials studied, showing the best electrocatalytic activity (smallest ASR) and good thermochemical and electrochemical stability. Si-/P-substitution constitutes a promising and novel approach to improve a perovskite oxide's catalytic activity through exsolution.

2. METHODOLOGY

2.1. Computational Methods. The tetragonal (*I*4/*mcm*) structure of STO observed experimentally[14,16] was used for the computations. The spin-polarized generalized gradient approximation of Perdew, Burke, and Ernzerhof[25] was utilized for all calculations. The core electrons were handled through the projector augmented-wave method.[26] The Hubbard-*U* approach was used to treat the electronic localization of the Ti 3d and Ni 3d electrons with U_{eff} = 3.2 and 6.4 eV, respectively.[27] The energy cutoff was set to 520 eV for all calculations which were carried out using the Vienna Ab initio Simulation Package (VASP).[28]

2.1.1. Segregation Energetics: Slab Models. We calculated the Ni segregation energy in the STO slab models [2 × 1 × 1 cell, $Sr_{10}Ti_{10-x-y}Ni_x(Si/P)_yO_{26}$]. The energy and force convergence criteria were set at 10^{-6} eV and 0.02 eV/Å, respectively. The Brillouin zone was sampled on a 5 × 5 × 1 Monkhorst−Pack grid. A 20 Å vacuum layer was employed to prevent slab−slab interactions. First, we relaxed a tetragonal STO unit cell (20 atoms, $Sr_4Ti_4O_{12}$). Then, using this cell, we constructed the (100)-oriented slab model ($Sr_{10}Ti_{10}O_{26}$). We introduced different defects in the slabs representing different surface systems, where the cations in the bottom two layers were fixed according to the precomputed bulk phase, but the O sites were allowed to change atomic coordinates in relaxation, see more details regarding the slab models in Figures S2 and S3 and Note S2. The third layer represents the bulk of the

https://doi.org/10.1021/acs.energyfuels.1c01985
Energy Fuels XXXX, XXX, XXX−XXX

material, and the top two layers represent the second and uppermost surfaces, see Figure S3.

The segregation energy, E_{seg}, was computed using the following formula

$$E_{seg} = E_{surf} - E_{bulk} \quad (1)$$

where E_{bulk} and E_{surf} are the energies of the slabs with the segregated (exsolved) atom in layers 3 and 1, respectively (Figure S4). We used 1 to compute segregation energies for (i) Ni (E_{seg}^{Ni}); (ii) Si (E_{seg}^{Si}); and (iii) P (E_{seg}^{P}). We computed E_{seg}^{Ni} for defect $Si_{Ti}^{\times}$ or $P_{Ti}^{\bullet}$ in layers 1 (Figure S4a), 2 (Figure S4b), and 3 (Figure S4c), and these slabs were also used for E_{seg}^{Si} and E_{seg}^{P}. If $E_{seg} < 0$, then the B-site cation is likely to exsolve. In contrast, if $E_{seg} > 0$, then the B-site cation is unlikely to segregate toward the surface. For $E_{seg} < 0$, the smaller E_{seg} suggests a greater tendency of the B-site cation to egress.[16] To understand the physical mechanism of segregation, Bader charge analysis was performed.[29,30] We also calculated the net defect charge of Si_{Ti}^{z} and P_{Ti}^{z}, where z is the defect charge or the difference between Bader charge of Ti and the substituted Si or P for an atomic position, to determine if there is attractive or repulsive interactions between Ni_{Ti}'' and Si_{Ti}^{z}/P_{Ti}^{z}.

2.1.2. Climbing Image Nudged Elastic Band. To evaluate Ni migration energetics in the studied materials, the minimum-energy path (MEP) was computed using the CINEB method.[31] The energy and force convergence criteria were set at 10^{-4} eV and 0.1 eV/Å, respectively. The Brillouin zone was sampled on a 2 × 2 × 2 Monkhorst−Pack grid. Initially, we considered three different routes of Ni transportation in $Sr_{32-\alpha}Ti_{30}Ni_1O_{96-\beta}$ (160 lattice sites with a V_{Ti}'''' site for the Ni-site in the final state), a 2 × 2 × 2 supercell for MEP computation: (i) a Sr-vacancy-oriented path ($\alpha = 1$ and $\beta = 0$), see Figure S5a; (ii) an O-vacancy-oriented path ($\alpha = 0$ and $\beta = 1$), see Figure S5b; and (iii) a direct diagonal path ($\alpha = 0$ and $\beta = 0$), see Figure S5c. Then, we added $Si_{Ti}^{\times}$ and $P_{Ti}^{\bullet}$ defects in $Sr_{32}Ti_{29}Ni_1(Si/P)_1O_{96}$ to compute the Ni migration barrier with nonmetal defects.

2.1.3. DOS, Lattice Parameters, and Vacancy Formation Energies. We computed lattice parameters, DOS, and vacancy formation energies on 2 × 2 × 2 (160 lattice sites) supercells of ST90N ($Sr_{26}Ti_{29}Ni_3O_{87}$ approximating $Sr_{0.8}Ti_{0.9}Ni_{0.1}O_{2.7}$), ST85NS5 ($Sr_{26}Ti_{27}Ni_3Si_2O_{87}$ approximating $Sr_{0.8}Ti_{0.85}Ni_{0.1}Si_{0.05}O_{2.7}$), and ST85NP5 ($Sr_{26}Ti_{27}Ni_3P_2O_{88}$ approximating $Sr_{0.8}Ti_{0.85}Ni_{0.1}P_{0.05}O_{2.7}$), see details in Layout S1 and Note S3.[32] Also, ST80NS10 ($Sr_{0.8}Ti_{0.8}Ni_{0.1}Si_{0.1}O_{2.7}$ approximating $Sr_{26}Ti_{26}Ni_3Si_3O_{87}$) and ST80NP10 ($Sr_{0.8}Ti_{0.8}Ni_{0.1}P_{0.1}O_{2.725}$ approximating $Sr_{26}Ti_{26}Ni_3P_3O_{88}$) supercells were used for computing the lattice parameters. The energy and force convergence criteria were set at 10^{-4} eV and 0.1 eV/Å, respectively. The Brillouin zone was sampled on a 2 × 2 × 2 Monkhorst−Pack grid, which was increased to 3 × 3 × 3 for DOS computations.

We searched for the most energetically stable $V_O^{\bullet\bullet}$ site in the charge-neutral ST90N, ST85NS5, and ST85NP5 to compute the formation energy, E_{vac} of $V_O^{\bullet\bullet}$, defined[33,34] as

$$E_{vac} = E_{def} - E_i + \frac{\Delta\mu_{O_2}}{2} + \frac{1}{2}\Delta h_O \quad (2)$$

where E_{def} and E_i are the energies of the defective structure (with a $V_O^{\bullet\bullet}$) and the pristine structure, respectively; Δh_O is the O_2 overbinding correction term (1.36 eV);[27] and $\Delta\mu_{O_2}$ is the chemical potential of gaseous O_2 at various temperatures (T) and oxygen partial pressures (pO_2)[35] and was defined as

$$\Delta\mu_{O_2}(T, p) = \Delta\mu_{O_2}^{0}(T, p^0) + RT\left(\frac{pO_2}{p^0}\right) \quad (3)$$

where $\Delta\mu_{O_2}^{0}$ is the chemical potential of gaseous O_2 at 1 atm of pO_2 (p^0) and R is the gas constant taken as 8.62×10^{-5} eV/K.

2.2. Experimental Methods. *2.2.1. Synthesis.* We prepared all ceramics using the solid-state reaction method. Stoichiometric amounts of $SrCO_3$, TiO_2, NiO, and SiO_2 (for Si-substituted samples) or $NH_4H_2PO_4$ (for P-substituted samples) were mixed in ethanol and ball-milled (Planetary Ball Mill, XQM-0.4A). The slurry was then dried and pressed isostatically (~200 MPa) into pellets. The pellets were then calcined in air for 12 h at 1300 °C. After that, the resulting pellets were crushed and ball-milled to obtain the ceramic powder. $Sr_{0.8}Ti_{0.9}Ni_{0.1}O_{3-\delta}$ (ST90N) was prepared using the same method with the sintering temperature set at 1400 °C, consistent with the literature.[16] For exsolution imaging, ST85NS5 powders were ball-milled with 10 wt % activated carbon, cold-pressed (~50 MPa), and calcined at 1300 °C for 5 h. The samples were then broken into smaller pieces and reduced at 800 °C with ~4 sccm of dry H_2 for up to 100 h.

2.2.2. X-ray Diffraction. All powders were analyzed by powder X-ray diffraction (XRD) using a PANalytical X'pert Pro instrument with a Cu Kα radiation source (λ = 1.5406 Å). Rietveld refinement was used to identify the crystal structure of the materials. ST85NS5 and ST85NP5 were also characterized as a function of temperature by high-temperature XRD (HT-XRD) from room temperature to 800 °C with an interval of 100 °C and a ramping rate of 5 °C/min. The HT-XRD 2θ scan ranged from 10 to 90° with a step of 0.02°. To check whether the phase of the host lattice changed after Ni exsolution, the structural changes of ST85NS5 under operational conditions (3% humidified H_2) were evaluated with XRD. In this test, ST85NS5 powder was kept in two isothermal cycles (at 800 °C), where each cycle was 15 h long. The 15 and 30 h reduced ST85NS5 samples were cooled down to room temperature before analyzing them with XRD.

2.2.3. Electron Microscopy. The surface and nanoparticle morphology of reduced samples were examined by using scanning electron microscopy (SEM) and energy-dispersive X-ray spectroscopy (EDX) using a JSM 6700F (JEOL) instrument. Then, the morphology and crystallinity of the reduced materials were examined by transmission electron microscopy (TEM) and selected-area electron diffraction (SAED)[36] with a JEM-2010F (JEOL) machine.

2.2.4. X-ray Photoelectron Spectroscopy and X-ray Fluorescence. The composition of the bulk was examined by X-ray fluorescence (XRF) using a JEOL JSX-3201Z instrument. The surface composition and elemental oxidation states were examined by X-ray photoelectron spectroscopy (XPS) using a PerkinElmer PHI 5600 instrument with a 150 W monochromatic Al Kα (1486.6 eV) source. A charge neutralizer (current = 1.7 A, balance = 2.2 V, and bias = 1.3 V) was used during XPS characterization. For each sample, a scan from 0 to 1400 eV with a 1 eV step was conducted with the pass energy set at 160 eV. A high-resolution scan was performed with 0.1 eV step and a 40 eV pass energy. The peaks were Shirley-background-subtracted and calibrated using adventitious carbon.

https://doi.org/10.1021/acs.energyfuels.1c01985
Energy Fuels XXXX, XXX, XXX−XXX

2.2.5. Electrochemical Testing. Four-probe direct current conductivity measurements were carried out on 15 mm × 5 mm × 2 mm bar-shaped samples. For the preparation of these samples, the ceramic powders were first ball-milled and then uniaxially and subsequently isostatically pressed (~250 MPa). Finally, the bars were re-sintered in air for 4 h at 1300 °C (1400 °C for ST90N).[16] The conductivity was measured in a 3% humidified H_2 environment at temperatures between 500 and 800 °C. The data were collected using a VSP BioLogic potentiostat. A constant current in the range of 0.005−1.400 mA was applied, and the potential difference across the bar was measured.

We fabricated symmetric cells (electrode thickness ~ 25 μm) for electrochemical impedance spectroscopy (EIS) measurements. First, the electrode powders were mixed with samarium-doped ceria (SDC, $Sm_{0.20}Ce_{0.80}O_{2-x}$, Fuelcellmaterials) with a mass ratio of 0.65:0.35. Second, isopropyl alcohol, ethylene glycol, and glycerin were added to the powder mixture (of SDC and electrode powder) and were ball-milled for 2 h to obtain the electrode slurry. Third, both sides of the 0.5 mm thick and dense SDC electrolyte disks were spray-coated with the slurry. After that, the symmetric cells were calcined at 1200 °C for 2 h. Both sides of the symmetric cells were then painted with gold paste and silver wires were attached to connect the cell to the outer circuit. Finally, the symmetric cells were placed in a testing furnace with a 3% humidified H_2 environment and temperature at 800 °C where the EIS measurements were carried out. The frequency range was set to be between 10 mHz and 100 kHz with five points per decade.

3. RESULTS AND DISCUSSION

3.1. Computations. To demonstrate the reducibility of A- and B-site elements, we computed Gibbs free energy change, ΔG between 100 and 1000 °C, see Figure S6a.[5,14,37] Only Ni has negative ΔG (−52.5 kJ mol^{-1} at 1000 °C), whereas the other A- and B-site elements have higher ΔG, supporting the idea that Ni exsolves and late transition metals can be easily reduced.

3.1.1. Segregation Energetics. DFT + U calculations using 1 on (100)-slab models gave negative E_{seg}^{Ni} values for all configurations, see Figure 1a,b. Si_{Ti}^{z} and P_{Ti}^{z} defects in layer 1 are positively charged (Figure 1c), so they attract the negatively charged Ni''_{Ti}. Conversely, Si_{Ti}^{z} and P_{Ti}^{z} in layers 2 and 3 are negatively charged, so they repel Ni''_{Ti}. An illustration is given in Figure S7a. In light of the electrostatic interaction, Si- or P-substituted configurations have smaller E_{seg}^{Ni} than the configuration without nonmetal, STN (its E_{seg}^{Ni} is −1.77 eV).

The slabs with Si_{Ti}^{z} in layer 1 have the smallest E_{seg}^{Ni} (−2.49 eV) compared to P_{Ti}^{z} in layer 1 (−1.93 eV). This could be due to a more positive Bader defect charge of Si_{Ti}^{z} (+0.20) than P_{Ti}^{z} (+0.12). The smaller Bader charge of P (1.98) compared to Si (2.06) in layer 1 (Figure S8b,c) could be due to the higher reducibility of P than Si. More details regarding the Bader charge analysis are given in Note S4. Both Si_{Ti}^{z} and P_{Ti}^{z} defects are positively charged because Ti in layer 1 of STN is coordinatively unsaturated (Figure S7b), which leads to a much lower Ti Bader charge (1.86) than in layers 2 (2.26) and 3 (2.27), see Figure S8a.[16] This larger nominal charge of Ti in the bulk also leads to negatively charged P_{Ti}^{z} and Si_{Ti}^{z} defects; Si_{Ti}^{z} is −0.17 and P_{Ti}^{z} is −0.18 in layer 2 and Si_{Ti}^{z} is −0.12 and P_{Ti}^{z} is −0.07 in layer 3. The smaller E_{seg}^{Ni} of Si_{Ti}^{z} and P_{Ti}^{z} in layer 2 (about −2.16 eV) compared to −2.00 eV for Si_{Ti}^{z} and −1.89 eV for P_{Ti}^{z} in layer 3 is due to the greater repulsion from the larger negative charges.

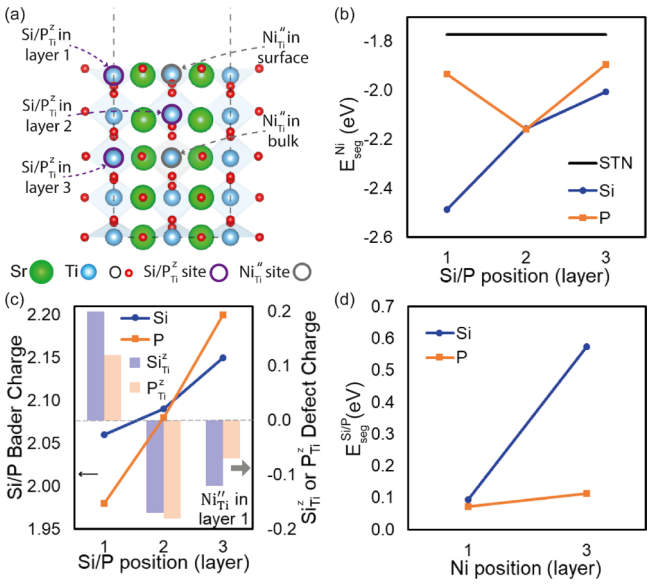

Figure 1. (a) The (100)-slab model shows the different atomic positions of Ni, Si, and P utilized for the segregation energy calculations. (b) Relative Ni segregation energy (E_{seg}^{Ni}) computed for slabs with Si or P atoms in different lattice positions (three different layers); the black line shows the E_{seg}^{Ni} of the slab without any nonmetal atoms (STN). (c) Bader charges of Si and P in three different layers when Ni''_{Ti} is in layer 1 and the computed defect charges for the Si/P_{Ti}^{z} defects shown with column bars in the right vertical axis. (d) Relative Si/P segregation energy ($E_{seg}^{Si/P}$) computed for slabs with Ni''_{Ti} fixed in two lattice positions (layers 1 and 3).

We also computed Si and P segregation energies (E_{seg}^{Si} and E_{seg}^{P}) using 1 and found that these two nonmetals are unlikely to segregate ($E_{seg}^{Si/P} > 0$), indicating that both Si_{Ti}^{z} and P_{Ti}^{z} are favored in the bulk compared to the surface, see Figure 1d. Both E_{seg}^{Si} and E_{seg}^{P} values (about 0.08 eV) with Ni''_{Ti} in layer 1 are smaller than the configurations with Ni''_{Ti} in layer 3 (E_{seg}^{Si} is 0.57 eV and E_{seg}^{P} is 0.11 eV). More details are given in Figure S7c and Note S5. These calculations suggest that nonmetals in Ni-substituted STO lower E_{seg}^{Ni}, showing promise for enhanced Ni-exsolution kinetics.

3.1.2. Climbing Image Nudged Elastic Band. We used CINEB to compute the impact of Si- and P-substitution on Ni migration barriers. Initially, we computed MEP for three possible Ni transport routes in $Sr_{32-\alpha}Ti_{30}Ni_1O_{96-\beta}$ (2 × 2 × 2 supercell): (i) a Sr-vacancy-oriented path (3.20 eV, Figure S5a); (ii) an O-vacancy-oriented path (4.02 eV, Figure S5b); and (iii) a direct diagonal path (4.51 eV, Figure S5c), see Figure S5e. The transport through Sr-vacancy (V''_{Sr}) is energetically preferred as the repulsion between large positively charged Sr^{2+} and positive Ni^{2+} is absent. The O-vacancy ($V_O^{\bullet\bullet}$) path provides the shortest distance for Ni transport between B-sites, but the repulsion between positively charged $V_O^{\bullet\bullet}$ and Ni^{2+} makes this path more energy-intensive than the V''_{Sr} route. We also computed MEP in $Sr_{32}Ti_{29}Ni_1(Si/P)_1O_{96}$ (Figure S5d) and found that the presence of Si and P lowers the Ni migration barrier from 4.51 to 4.31 and 4.20 eV, respectively (Figure 2a). In fact, the formation of the tetrahedral sublattices (SiO_4^{4-} and PO_4^{3-}) upon substitution[21−23] relative to the TiO_6^{8-}-octahedra can cause a slight distortion in the Ni sublattice (Figure S9). As mentioned previously (in Figure S1),

https://doi.org/10.1021/acs.energyfuels.1c01985
Energy Fuels XXXX, XXX, XXX−XXX

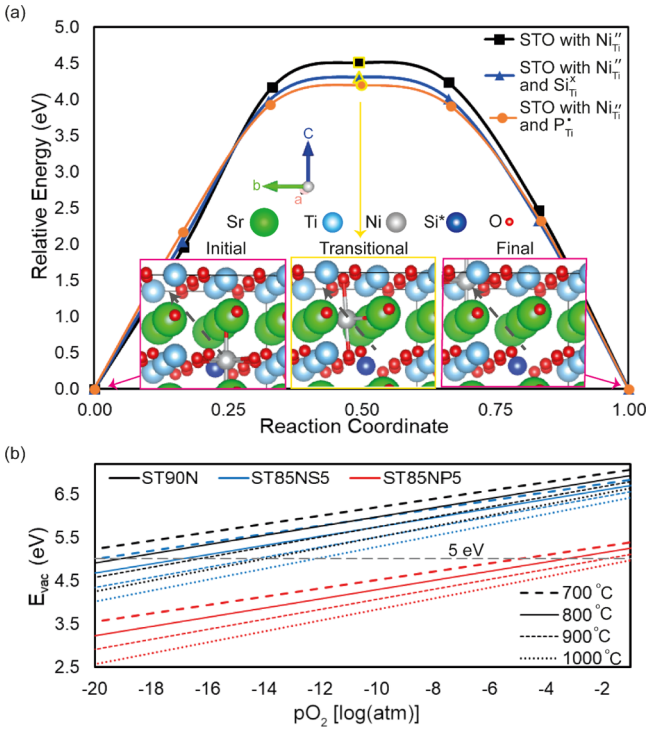

Figure 2. (a) CI-NEB results for Ni-migration in STO without any nonmetal defect and with $Si^{\times}_{Ti}$ or $P^{\bullet}_{Ti}$ near the initial Ni''_{Ti} site. The inset images inside the plot show the initial, transitional, and final ground states (the images of STO configuration with Ni''_{Ti} and $Si^{\times}_{Ti}$ are shown, *the same atomic position is used for $P^{\bullet}_{Ti}$). (b) Oxygen vacancy formation energies computed from ST90N, ST85NS5, and ST85NP5. $\Delta\mu_{O_2}$ is computed as a function of temperature and pO_2.

this distortion can be attributed to a weakened Ni−O bond which supports the lower Ni migration barrier in $Sr_{32}Ti_{29}Ni_1(Si/P)_1O_{96}$. P ($\chi$ = 2.19) is more electronegative than Si (χ = 1.90), so Ni in the $P^{\bullet}_{Ti}$-containing material has a lower charge (1.35 vs 1.40). The lower Ni valence correlates to a weaker Ni−O bond which results in a lower Ni migration barrier of the $P^{\bullet}_{Ti}$ configuration than the $Si^{\times}_{Ti}$ configuration.

3.1.3. Vacancy Formation Energies. Under reducing conditions, smaller E_{vac} for $V^{\bullet\bullet}_{O}$ formation correlates to the ease of Ni−O bond breaking and is in turn linked to enhanced exsolution kinetics.[16,38] We studied the formation of $V^{\bullet\bullet}_{O}$ using the 2 × 2 × 2 supercells (ST90N, ST85NS5, and ST85NP5) described in Section 2.1.3. We computed E_{vac} using 2 with $\Delta\mu_{O_2}$ computed for variable temperature and pO_2 using 3, which produced the following order for E_{vac}: ST90N > ST85NS5 > ST85NP5, see Figure 2b. ST85NP5 forms $V^{\bullet\bullet}_{O}$ more readily, and the lower E_{vac} is because $P^{\bullet}_{Ti}$ can reduce the material more than $Si^{\times}_{Ti}$, see defect equations in Note S6a. The largest pO_2 with $E_{vac} \leq 5$ eV is tabulated in Table S1, suggesting the pO_2 required for $V^{\bullet\bullet}_{O}$ to form at different temperatures (Note S6b).[34] In a 10^{-19} atm environment, at least 800 °C is required for ST90N and ST85NS5 to form $V^{\bullet\bullet}_{O}$, and ST85NP5 will form $V^{\bullet\bullet}_{O}$ at much lower temperatures. The lowest E_{vac} of ST85NP5 predicts better exsolution and better electrical conductivity performance than ST85NS5 and ST90N.[38,39]

3.1.4. Density of States. We computed the DOS and projected DOS using ST90N, ST85NS5, and ST85NP5 supercells; details can be found in Figure S10 and Note S7. These materials show a semiconducting behavior (Figure S10a), and the substitution of nonmetals lowers the band gap from 1.94 eV (ST90N) to 1.90 eV for ST85NS5 and 1.89 eV for ST85NP5. We also observed a minor increase in Fermi energies from 2.40 eV for ST90N to 2.50 eV for ST85NP5 and 2.60 eV for ST85NS5.

3.2. Experiments. *3.2.1. Structural Characterizations.* XRD characterization was performed to identify the structure of the samples listed in Table 1, including ST90N, ST85NS5, ST80NS10, and ST90NS5 (Figure 3a) and ST85NP5, ST80NP10, and ST90NP5 (Figure 3b). The nonstoichiometry in the Sr sublattice (i.e., A-site deficiency) causes the phase to be tetragonal (rather than the ideal cubic phase of STO).[14,16] In fact, all seven samples had the *I*4/*mcm* tetragonal phase as the primary phase with traces of impurities, including rutile TiO_2[16,40] and $NiTiO_3$ ($R\bar{3}$),[41,42] consistent with the literature.[16,40−42] The ST90N, ST85NS5, and ST85NP5 samples have a relatively high amount of the *I*4/*mcm* primary phase (≥94%). Increasing the Si and P concentrations to 10% decreases the primary phase to about 91 and 90% for ST80NS10 and ST80NP10, respectively. Due to the increased A-site deficiency, ST90NS5 and ST90NP5 exhibited secondary phases in the range between 8 and 12%, including an *Ama*2 SiO_2 phase (Materials Project: mp-554573) in ST90NS5.

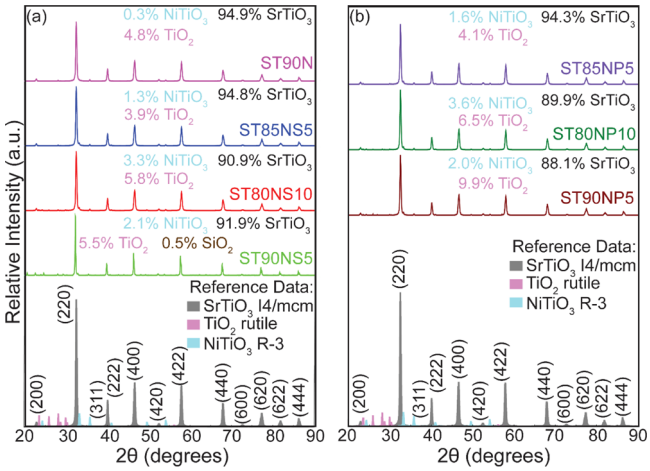

Figure 3. XRD patterns measured after sintering for (a) ST90N, ST85NS5, ST80NS10, and ST90NS5, the pristine sample and samples with different degrees of the Si-substituent, and (b) ST85NP5, ST80NP10, and ST90NP5, samples with different degrees of the P-substituent.

We tabulated the unit cell parameters obtained from XRD and DFT in Table 2. In the unit cells computed from experimental data, a lattice expansion occurred for 5% substitution (ST85NS5 and ST85NP5), followed by contraction for 10% substitution (ST80NS10 and ST80NP10), as shown in Figure S11. The lattice expansion in ST85NS5 and ST85NP5 could be due to the increase in the ionic radius of the B-site (Ti and Ni) because of partial reduction upon the introduction of $Si^{\times}_{Ti}$ or $P^{\bullet}_{Ti}$ (Figure S12a).[21−23] The lattice contraction in ST80NS10 and ST80NP10 (relative to ST85NS5 and ST85NP5) could be due to (i) higher doping of the smaller ionic radii of Si^{4+} (0.260 Å) or P^{5+} (0.170 Å) than Ti^{4+} (0.605 Å)[24] and (ii) the B-site expansion (from the partial reduction by $Si^{\times}_{Ti}$ and $P^{\bullet}_{Ti}$) is induced over less mol.% (90 from 95%), see Figure S12b. More details are given in Note S8a. Similar lattice changes were observed in the related studies.[21−23,43] We observed the same trend from DFT, where

https://doi.org/10.1021/acs.energyfuels.1c01985
Energy Fuels XXXX, XXX, XXX−XXX

Table 2. Calculated Unit Cell Parameters from the Rietveld Refinement of XRD Patterns along with the DFT-Computed Lattice Parameters Calculated from the 2 × 2 × 2 Supercells[a,b]

	ST90N	ST85NS5	ST80NS10	ST90NS5	ST85NP5	ST80NP10	ST90NP5
			XRD				
a (Å) = b (Å)	5.519	5.517	5.521	5.520	5.517	5.521	5.521
c (Å)	7.815	7.832	7.811	7.809	7.836	7.812	7.809
V (Å^3)	238.1	238.4	238.1	238.0	238.6	238.2	238.1
Δvol. (%)	0	0.13	0.01	−0.03	0.21	0.04	−0.004
			DFT				
a (Å) = b (Å)	5.525	5.519	5.528		5.520	5.529	
c (Å)	7.880	7.912	7.878		7.917	7.879	
V (Å^3)	240.5	241.0	240.7		241.2	240.9	
Δvol. (%)	0	0.22	0.10		0.30	0.17	
Δvol. [DFT−XRD] (%)	1.02	1.11	1.11		1.12	1.15	

[a]The first and second "Δvol." rows represent the volume compared with XRD-measured ST90N and the DFT-computed ST90N, respectively. [b]The last row shows the difference between XRD-measured and DFT-calculated lattice volumes.

the cell undergoes lattice expansion upon 5% substitution (by 0.22% for ST85NS5 and 0.30% for ST85NP5), followed by a contraction for 10% substitution (by 0.12% for ST80NS10 and 0.13% for ST80NP10). Additional details regarding the DFT computations are given in Note S8b and Figure S13.

We assessed the ST85NS5's and ST85NP5's thermal stability and TEC as anodes using HT-XRD, see Figures S14 and S15. Both samples did not exhibit detectable phase changes (Note S9a). We calculated TECs from HT-XRD lattice parameters in the 200−800 °C range using 100 °C as the initial reference temperature, see Table 3. The average

Table 3. TECs of ST85NS5 and ST85NP5 in the Temperature Range of 200−800 °C

units: 10^{-6} K^{-1}		along a-axis	along c-axis	unit cell volume
linear	ST85NS5	13.2	12.5	39.1
average TEC	ST85NP5	12.6	12.3	37.7

TECs of ST85NS5 and ST85NP5 are 39.1 × 10^{-6} K^{-1} and 37.7 × 10^{-6} K^{-1}, respectively. In comparison, STO and SDC have TECs of 9.4 × 10^{-6} K^{-1} and 15 × 10^{-6} K^{-1}, respectively.[44] Despite the high TEC, after 100 h of measurement at 800 °C in 3% humidified H_2, we did not observe any mechanical failure. We further confirmed the materials' stability in 3% humidified H_2 (methodology in Section 2.2.2), where we did not observe phase change upon exsolution of metallic Ni, see Figure S16 and Note S9b.[45] Moreover, SAED supported that the host lattice maintained its structural integrity after reduction, see Figure S17 and Note S9c.

3.2.2. X-ray Photoelectron Spectroscopy. 3.2.2.1. XPS Study: Si/P Substitution Level. The elemental composition of all samples matched the nominal values as evidenced by XPS and XRF characterizations (Table S2 and Note S10a).[46,47] XPS was utilized to examine the oxidation state of elements near the surface. The Ni 2p binding energies decrease upon 5% substitution (ST85NS5 and ST85NP5) and then increase when increasing the substituent concentration to 10% (ST80NS10 and ST80NP10), see Figures 4a and S18. The decrease in Ni's binding energy upon 5% substitution is attributed to the partial reduction of Ni (Note S6a). The induced reduction was only observed in Ni 2p, as Ti 2p binding energy changes were extremely small (ΔB.E. is 0.03 eV), Figure S19. This is supported by the greater reducibility

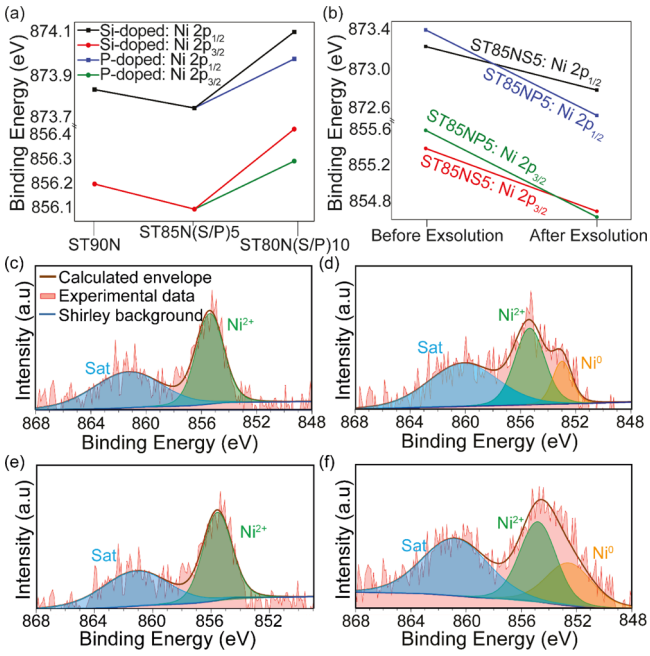

Figure 4. (a) Binding energy changes of Ni $2p_{1/2}$and Ni $2p_{3/2}$ spin−orbital components for different substitution concentrations for Si- and P-substituted samples compared with ST90N. (b) Binding energy changes of Ni $2p_{1/2}$ and Ni $2p_{3/2}$ spin−orbital components for ST85NS5 and ST85NP5 upon exsolution of Ni. The Ni $2p_{3/2}$ spin−orbital component's XPS spectra of (c) ST85NS5 before reduction, (d) ST85NS5 after reduction, (e) ST85NP5 before reduction, and (f) ST85NP5 after reduction, where the deconvoluted Ni^{2+} and Ni^0 components are shown.

of Ni^{2+} compared to that of Ti^{4+} (Note S10b).[48] The increase in Ni's binding energies upon 10% substitution is attributed to the c-contraction[49−51] observed in Section 3.2.1, see explanation given in Note S10c. In a relevant study,[22] nonmetal substitution induced both partial reduction and oxidation of B-site cations from different substitution levels. More importantly, the decreased binding energy of Ni upon 5% Si-/P-substitution suggests weakened Ni−O which can aid in breaking Ni−O during exsolution. We also examined the XPS spectra of Si 2p and P 2s peaks, which characterized their expected B-site sublattices, SiO_4^{4-} and PO_4^{3-}, see Figure S20 and Note S11. The significant peak areas associating with the

https://doi.org/10.1021/acs.energyfuels.1c01985
Energy Fuels XXXX, XXX, XXX−XXX

tetrahedral B-site sublattices suggest that the nonmetals are incorporated in the host lattice.

3.2.2.2. XPS after Exsolution. It is crucial to study the XPS analysis of Ni 2p peaks before and after reduction to confirm the exsolution of Ni. We added activated carbon (10 wt %) to both ST85NS5 and ST85NP5 and then reduced the samples in dry H_2 at 800 °C. After adding activated carbon, both samples showed a lower binding energy (before reduction), see Figure 4a,b. After reduction, we observed peaks associated with Ni^0 at 852.8 and 852.6 eV binding energies for ST85NS5 and ST85NP5, respectively (Figure 4c–f). The Ni $2p_{3/2}$ core peak deconvolutes to peak areas of 26.2 and 37.5% for the Ni^0 component for ST85NS5 and ST85NP5, respectively. Moreover, the Ni $2p_{1/2}$ and Ni $2p_{3/2}$ core peaks shift toward lower binding energies, suggesting the reduction of Ni (Figure 4b). We also noticed a peak broadening effect, suggesting bonding changes.[52] These Ni 2p XPS data support the notion that the exsolved particles consist of metallic Ni. Furthermore, we studied the Si 2p and P 2s spectra, see details in Figure S21 and Note S12.[53,54]

3.2.3. Electrochemical Tests. 3.2.3.1. Electrical Conductivity. We used the four-probe DC method in 3% humidified H_2 to measure the electrical conductivity of ST90N, ST85NS5, and ST85NP5 in a temperature range between 500 and 800 °C, see Figure 5. While ST90N and ST85NS5 have similar

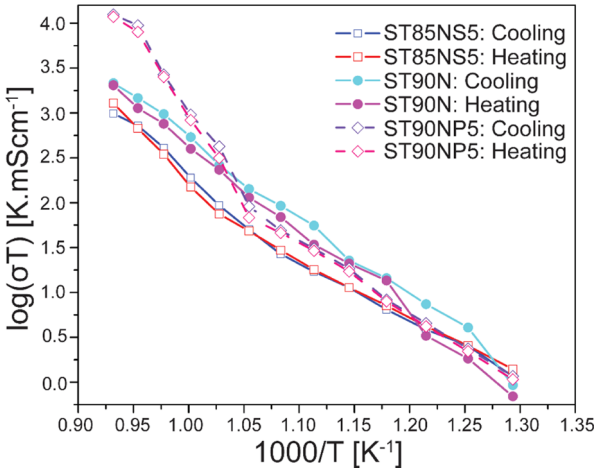

Figure 5. Conductivity of listed materials measured in 3% humidified H_2 with the four-probe DC method. "heating" and "cooling" in the legend means the temperature was increasing and decreasing, respectively, between temperature intervals while the measurements were taken.

conductivities of 1.9 and 1.2 mS cm^{-1} at 800 °C, respectively, ST85NP5 has a better electrical conductivity of 15.6 mS cm^{-1} at 800 °C. The electrical conductivity at lower temperatures (500–650 °C) is similar for all the measured materials, as predicted by the similar band gaps in the computed DOS. The improved conductivity of ST85NP5 at higher temperatures (700–800 °C) could be due to the donor-type nature of P-substitution. The electrical conductivity of 15.6 mS cm^{-1} for ST85NP5 and 1.2 mS cm^{-1} for ST85NS5 was stable for 100 h in the same 3% humidified H_2 environment at 800 °C (Figure 6a).

3.2.3.2. Area-Specific Resistance. We measured and characterized the ASR of the symmetric cells (Figure S22) in 3% humidified H_2, deconvolving the distribution relaxation

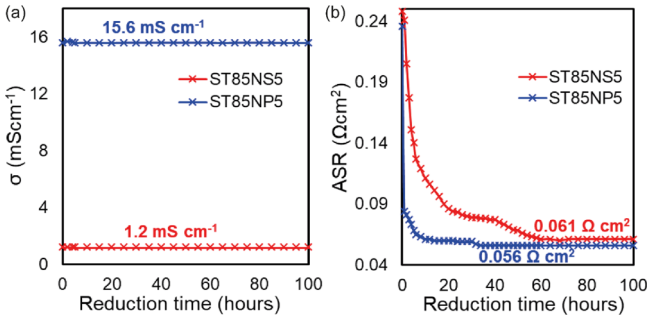

Figure 6. (a) Four-probe DC conductivities and (b) ASR values of ST85NS5 and ST85NP5 as a function of time and carried out in 3% humidified H_2 at 800 °C.

times (DRTs)[55–57] from the EIS data. Initially, to set apart the poor-performing samples compared to ST90N, we measured the ASR values of all the samples for about 10 h at 800 °C. We found improved ASR values in ST85NS5 and ST85NP5, whereas ST80NS10, ST90NS5, ST80NP10, and ST90NP5 had increasing ASR, see Figure S23a and Note S13a. The improved ASR of ST85NS5 and ST85NP5 compared to that of ST80NS10 and ST80NP10 could be due to (i) the weakened Ni–O bond observed upon 5% Si- and P-substitution and (ii) the strengthened Ni–O bond observed upon 10% nonmetal substitution, see Figure S23b and Note S13b. Weakened Ni–O suggests that easier exsolution is expected with 5% Si- and P-substituted samples rather than 10% substitution.

By integrating the deconvolved DRTs of ST85NS5 (Figure S24) and ST85NP5 (Figure S25) from the EIS data measured after 100 h at 800 °C, along the log of the timescales, we computed the ASR (Figure 6b). The ASR of ST85NS5 decreased from 0.248 to 0.061 Ω cm^2 before the 60 h mark. Similarly, ST85NP5's ASR decreased from 0.236 to 0.056 Ω cm^2 after 30 h. Both ST85NS5 and ST85NP5 samples showed a constant ASR for about 40 and 70 h, respectively. The DRT showed three distinctive processes associated with high (800 Hz), medium (18 Hz), and low (0.15 Hz) frequencies approximately, see Figures S24 and S25 and Table S3. The low-frequency component contributes to most of the impedance, see details in Note S13c.[58–60] The improved ASR values of ST85NS5 and ST85NP5 compared to that of ST90N agree with the computations showing energetically favored Ni segregation and lower Ni migration barrier in CINEB. ST85NP5's faster decrease rate and lower ASR compared to ST85NS5 can be attributed to its lower E_{vac} value and Ni migration barrier.

3.2.4. Nanoparticle Analysis. We reduced ST85NS5 in dry H_2 to analyze the exsolved nanoparticles at different time intervals. Figure 7a,b shows the SEM images of a 100 h reduced sample and its corresponding EDX image of Ni nanoparticles. Exsolution was expected to occur readily in the reducing environment; the 5 h reduced sample (Figure 7d) had several small nanoparticles (~30 nm) compared to Figure 7c (before reduction). After 35 h of reduction (Figure 7e), we found large nanoparticles (~250 nm) with a size comparable to that observed after 100 h of reduction (Figure 7f). Some nanoparticles, having reached the maximum size at 35 h, may explain the slower decrease rate of ASR. The 100 h reduced sample had well-distributed nanoparticles on the surface, with diameters ranging from 50 to 250 nm (Figure 7f). Moreover, we observed more particles at grain boundaries, see Figure S26.

https://doi.org/10.1021/acs.energyfuels.1c01985
Energy Fuels XXXX, XXX, XXX–XXX

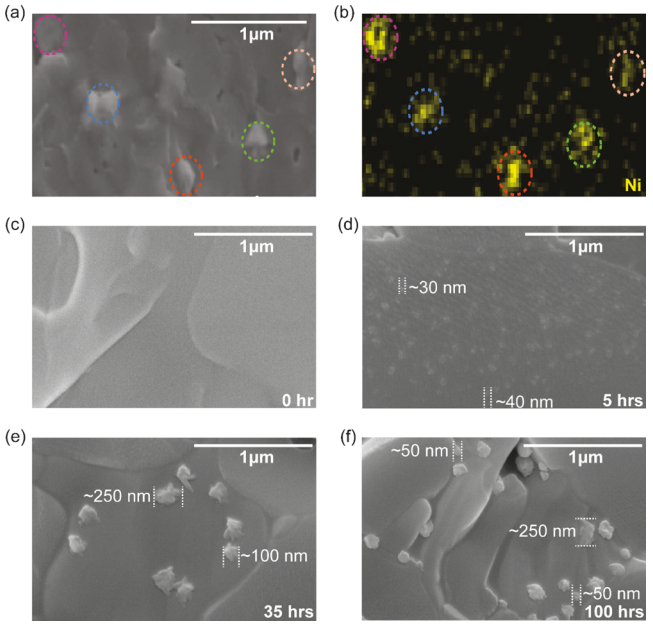

Figure 7. (a) SEM and (b) EDX images of the ST85NS5 sample reduced in dry H_2 at 800 °C. Exsolved Ni nanoparticles are highlighted. The SEM images in (c–f) indicate the growth of nanoparticles. (c) The surface without exsolved particles before reduction, (d) the surface after 5 h of reduction populated with smaller nanoparticles, (e) the surface after 35 h of reduction, with some nanoparticles having reached the maximum size, and (f) the surface after 100 h of reduction with various sizes of nanoparticles.

4. CONCLUSIONS

This work shows that small levels of Si- or P-substitution in the B-site of STO enhance the electrochemical performance and Ni-exsolution kinetics. The DFT + U computations show that the Ni segregation, Ni diffusion, and E_{vac} improve by Si- and P-substitution. P is a slightly better nonmetal substituent than Si, demonstrating better Ni-exsolution kinetics (with lower Ni transportation barrier and E_{vac}). The computational findings were validated against experiments, and we found that 5% Si-/P-substitution provided the best performance among the compositions tested. The partial reduction of Ni upon 5% Si- and P-substitution (shown with Ni 2p XPS) suggests a weakening of the Ni–O bond, potentially improving the exsolution kinetics (in ST85NS5 and ST85NP5). However, upon 10% substitution, we observed a strengthened Ni–O bond, leading to decreased Ni migration kinetics as reflected in ST80NS10's and ST80NP10's increased ASR with reduction time. The XRD analysis and DFT support this hypothesis by showing a lattice expansion upon 5% substitution and contraction upon 10% substitution. The enhanced catalytic performance of 0.061 Ω cm^2 by ST85NS5 and 0.056 Ω cm^2 by ST85NP5 is a leap from the 0.600 Ω cm^2 of the pristine material ST90N. Furthermore, ST85NS5 and ST85NP5 demonstrated thermochemical stability, retaining or improving their ASR values during 100 h tests. The improvement by Si- and P-substitution is encouraging for similar perovskites to enhance the catalytic activity.

■ ASSOCIATED CONTENT

Supporting Information

The Supporting Information is available free of charge at https://pubs.acs.org/doi/10.1021/acs.energyfuels.1c01985.

Ni transportation barrier for Sr-vacancy- and O-vacancy-oriented paths compared with the direct diagonal path; largest pO_2 with $E_{vac} \leq 5$ eV and DOS computations for the 5% Si- and P-substituted 2 × 2 × 2 supercell compared with a supercell without nonmetal defects; XRD-measured lattice parameter changes upon different degrees of Si- and P-substitution; lattice parameters and the distortion index for DFT-computed supercells; HT-XRD analyses of 5% Si- and P-substituted samples; XRD, TEM, and SAED images of the reduced 5% Si-doped material; elemental compositions measured by XPS and XRF; Ni 2p and Ti 2p XPS for the degree of Si- and P-substitution; Si 2p and P 2s XPS for different degrees of substitution and changes after reduction; ASR of all the tested samples; and DRTs of 5% Si- and P-substituted samples (PDF)

■ AUTHOR INFORMATION

Corresponding Author

Francesco Ciucci − *Department of Mechanical and Aerospace Engineering, The Hong Kong University of Science and Technology, Kowloon 999077 Hong Kong SAR, China; Department of Chemical and Biological Engineering, The Hong Kong University of Science and Technology, Kowloon 999077 Hong Kong SAR, China;* orcid.org/0000-0003-0614-5537; Email: francesco.ciucci@ust.hk

Authors

Md Raziun Bin Mamtaz − *Department of Mechanical and Aerospace Engineering, The Hong Kong University of Science and Technology, Kowloon 999077 Hong Kong SAR, China*

Zheng Wang − *Department of Mechanical and Aerospace Engineering, The Hong Kong University of Science and Technology, Kowloon 999077 Hong Kong SAR, China;* orcid.org/0000-0002-7560-2618

Alessio Belotti − *Department of Mechanical and Aerospace Engineering, The Hong Kong University of Science and Technology, Kowloon 999077 Hong Kong SAR, China*

Emanuele Quattrocchi − *Department of Mechanical and Aerospace Engineering, The Hong Kong University of Science and Technology, Kowloon 999077 Hong Kong SAR, China*

Jing Yu − *Department of Mechanical and Aerospace Engineering, The Hong Kong University of Science and Technology, Kowloon 999077 Hong Kong SAR, China*

Jiapeng Liu − *Department of Mechanical and Aerospace Engineering, The Hong Kong University of Science and Technology, Kowloon 999077 Hong Kong SAR, China;* orcid.org/0000-0001-8667-1929

Complete contact information is available at: https://pubs.acs.org/10.1021/acs.energyfuels.1c01985

Notes

The authors declare no competing financial interest.

■ ACKNOWLEDGMENTS

This project was financially supported by the Research Grants Council (GRF Projects: 16201820 and 16206019). The authors appreciate the technical assistance from the Advanced Engineering Materials facilities (AEMF) and the Materials Characterization and Preparation Facilities (MCPF) of HKUST. The calculations were performed on the Tianhe-2

https://doi.org/10.1021/acs.energyfuels.1c01985
Energy Fuels XXXX, XXX, XXX−XXX

supercomputer system in Guangzhou. A.B. and E.Q. thank the Hong Kong Ph.D. Fellowship Scheme for its support.

REFERENCES

(1) Singhal, S. Solid Oxide Fuel Cells for Stationary, Mobile, and Military Applications. *Solid State Ionics* **2002**, *152*−*153*, 405−410.
(2) Cooper, S. J.; Brandon, N. P. *Solid Oxide Fuel Cell Lifetime and Reliability: Critical Challenges in Fuel Cells*; Elsevier Ltd., 2017, Chapter 1, pp 1−18.
(3) Wang, W.; Su, C.; Wu, Y.; Ran, R.; Shao, Z. Progress in Solid Oxide Fuel Cells with Nickel-Based Anodes Operating on Methane and Related Fuels. *Chem. Rev.* **2013**, *113*, 8104−8151.
(4) Boldrin, P.; Brandon, N. P. Progress and Outlook for Solid Oxide Fuel Cells for Transportation Applications. *Nat. Catal.* **2019**, *2*, 571−577.
(5) Gao, Y.; Chen, D.; Saccoccio, M.; Lu, Z.; Ciucci, F. From Material Design to Mechanism Study: Nanoscale Ni Exsolution on a Highly Active A-site Deficient Anode Material for Solid Oxide Fuel Cells. *Nano Energy* **2016**, *27*, 499−508.
(6) Sun, Y.-F.; Zhang, Y.-Q.; Chen, J.; Li, J.-H.; Zhu, Y.-T.; Zeng, Y.-M.; Amirkhiz, B. S.; Li, J.; Hua, B.; Luo, J.-L. New Opportunity for in situ Exsolution of Metallic Nanoparticles on Perovskite Parent. *Nano Lett.* **2016**, *16*, 5303−5309.
(7) Aricò, A. S.; Bruce, P.; Scrosati, B.; Tarascon, J.-M.; van Schalkwijk, W. Nanostructured Materials for Advanced Energy Conversion and Storage Devices. *Nat. Mater.* **2005**, *4*, 366−377.
(8) Rossmeisl, J.; Bessler, W. G. Trends in Catalytic Activity for SOFC Anode Materials. *Solid State Ionics* **2008**, *178*, 1694−1700.
(9) Shiozaki, R.; Andersen, A. G.; Hayakawa, T.; Hamakawa, S.; Suzuki, K.; Shimizu, M.; Takehira, K. Partial Oxidation of Methane over a Ni/BaTiO3 Catalyst Prepared by Solid Phase Crystallization. *J. Chem. Soc., Faraday Trans.* **1997**, *93*, 3235−3242.
(10) Neagu, D.; Oh, T.-S.; Miller, D. N.; Ménard, H.; Bukhari, S. M.; Gamble, S. R.; Gorte, R. J.; Vohs, J. M.; Irvine, J. T. S. Nano-socketed Nickel Particles with Enhanced Coking Resistance grown in situ by redox exsolution. *Nat. Commun.* **2015**, *6*, 8120.
(11) Nishihata, Y.; Mizuki, J.; Akao, T.; Tanaka, H.; Uenishi, M.; Kimura, M.; Okamoto, T.; Hamada, N. Self-regeneration of a Pd-perovskite Catalyst for Automotive Emissions Control. *Nature* **2002**, *418*, 164−167.
(12) Madsen, B. D.; Kobsiriphat, W.; Wang, Y.; Marks, L. D.; Barnett, S. A. Nucleation of Nanometer-scale Electrocatalyst Particles in Solid Oxide Fuel Cell Anodes. *J. Power Sources* **2007**, *166*, 64−67.
(13) Kim, J. H.; Kim, J. K.; Liu, J.; Curcio, A.; Jang, J.-S.; Kim, I.-D.; Ciucci, F.; Jung, W. Nanoparticle Ex-solution for Supported Catalysts: Materials Design, Mechanism and Future Perspectives. *ACS Nano* **2020**, *15*, 81−110.
(14) Neagu, D.; Tsekouras, G.; Miller, D. N.; Ménard, H.; Irvine, J. T. S. In situ Growth of Nanoparticles Through Control of Non-stoichiometry. *Nat. Chem.* **2013**, *5*, 916−923.
(15) Neagu, D.; Irvine, J. T. S. Structure and Properties of La0.4Sr0.4TiO3 Ceramics for Use as Anode Materials in Solid Oxide Fuel Cells. *Chem. Mater.* **2010**, *22*, 5042−5053.
(16) Gao, Y.; Lu, Z.; You, T. L.; Wang, J.; Xie, L.; He, J.; Ciucci, F. Energetics of Nanoparticle Exsolution from Perovskite Oxides. *J. Phys. Chem. Lett.* **2018**, *9*, 3772−3778.
(17) Setoguchi, T.; Okamoto, K.; Eguchi, K.; Arai, H. Effects of Anode Material and Fuel on Anodic Reaction of Solid Oxide Fuel Cells. *J. Electrochem. Soc.* **1992**, *139*, 2875−2880.
(18) Yang, L.; Xie, K.; Xu, S.; Wu, T.; Zhou, Q.; Xie, T.; Wu, Y. Redox-reversible Niobium-Doped Strontium Titanate Decorated with in situ Grown Nickel Nanocatalyst for High-temperature Direct Steam Electrolysis. *Dalton Trans.* **2014**, *43*, 14147−14157.
(19) Chan, N.-H.; Sharma, R. K.; Smyth, D. M. Nonstoichiometry in $SrTiO_3$. *J. Electrochem. Soc.* **1981**, *128*, 1762−1769.
(20) Marina, O. A.; Canfield, N. L.; Stevenson, J. W. Thermal, Electrical, and Electrocatalytical Properties of Lanthanum-doped Strontium Titanate. *Solid State Ionics* **2002**, *149*, 21−28.
(21) Hancock, C. A.; Slade, R. C. T.; Varcoe, J. R.; Slater, P. R. Synthesis, Structure and Conductivity of Sulfate and Phosphate Doped $SrCoO_3$. *J. Solid State Chem.* **2011**, *184*, 2972−2977.
(22) Hancock, C. A.; Slater, P. R. Synthesis of Silicon Doped $SrMO_3$ (M = Mn, Co): Stabilization of the Cubic Perovskite and Enhancement in Conductivity. *Dalton Trans.* **2011**, *40*, 5599−5603.
(23) Hancock, C. A.; Porras-Vazquez, J. M.; Keenan, P. J.; Slater, P. R. Oxyanions in Perovskites: from Superconductors to Solid Oxide Fuel Cells. *Dalton Trans.* **2015**, *44*, 10559−10569.
(24) Shannon, R. D. Revised Effective Ionic Radii and Systematic Studies of Interatomic Distances in Halides and Chalcogenides. *Acta Crystallogr., Sect. A: Found. Adv.* **1976**, *32*, 751−767.
(25) Perdew, J. P.; Burke, K.; Ernzerhof, M. Generalized Gradient Approximation Made Simple. *Phys. Rev. Lett.* **1996**, *77*, 3865−3868.
(26) Blöchl, P. E. Projector Augmented-wave Method. *Phys. Rev. B: Condens. Matter Mater. Phys.* **1994**, *50*, 17953−17979.
(27) Wang, L.; Maxisch, T.; Ceder, G. Oxidation Energies of Transition Metal Oxides within the GGA+U Framework. *Phys. Rev. B: Condens. Matter Mater. Phys.* **2006**, *73*, 195107−195113.
(28) Kresse, G.; Hafner, J. Ab initio Molecular Dynamics for Liquid Metals. *Phys. Rev. B: Condens. Matter Mater. Phys.* **1993**, *47*, 558−561.
(29) Henkelman, G.; Arnaldsson, A.; Jónsson, H. A Fast and Robust Algorithm for Bader Decomposition of Charge Density. *Comput. Mater. Sci.* **2006**, *36*, 354−360.
(30) Limas, N. G.; Manz, T. A. Introducing DDEC6 Atomic Population analysis: Part 4. Efficient Parallel Computation of Net Atomic Charges, Atomic Spin Moments, Bond Orders, and More. *RSC Adv.* **2018**, *8*, 2678−2707.
(31) Henkelman, G.; Uberuaga, B. P.; Jónsson, H. Climbing Image Nudged Elastic Band Method for Finding Saddle Points and Minimum Energy Paths. *J. Chem. Phys.* **2000**, *113*, 9901−9904.
(32) Ong, S. P.; Richards, W. D.; Jain, A.; Hautier, G.; Kocher, M.; Cholia, S.; Gunter, D.; Chevrier, V. L.; Persson, K. A.; Ceder, G. Python Materials Genomics (pymatgen): A Robust, Open-source Python Library for Materials Analysis. *Comput. Mater. Sci.* **2013**, *68*, 314−319.
(33) Nayak, S. K.; Adeagbo, W. A.; Langhammer, H. T.; Hergert, W.; Müller, T.; Böttcher, R. Study of Charged Defects for Substitutionally Doped Chromium in Hexagonal Barium Titanate from First-principles Theory. *Phys. Status Solidi RRL* **2014**, *8*, 527−531.
(34) Liu, B.; Cooper, V. R.; Xu, H.; Xiao, H.; Zhang, Y.; Weber, W. J. Composition Dependent Intrinsic Defect Structures in $SrTiO_3$. *Phys. Chem. Chem. Phys.* **2014**, *16*, 15590−15596.
(35) Chase, M. W., Jr.; Davies, C. A.; Downey, J. R., Jr.; Frurip, D. J.; McDonald, R. A.; Syverud, A. N. NIST-JANAF Thermodynamical Tables Fourth Edition. *J. Phys. Chem. Ref. Data 14*, (**1998**) DOI: DOI: 10.18434/T42S31, NIST Standard Reference Database 13, Supplement no. 1. https://janaf.nist.gov/ (accessed: 2021-03-10).
(36) Lábár, J. L. Consistent Indexing of a (set of) Single Crystal SAED Pattern(s) with the ProcessDiffraction Program. *Ultramicroscopy* **2005**, *103*, 237−249.
(37) Tanaka, H.; Uenishi, M.; Taniguchi, M.; Tan, I.; Narita, K.; Kimura, M.; Kaneko, K.; Nishihata, Y.; Mizuki, J. The Intelligent Catalyst Having the Self-regenerative Function of Pd, Rh and Pt for Automotive Emissions Control. *Catal. Today* **2006**, *117*, 321−328.
(38) Kwon, O.; Sengodan, S.; Kim, K.; Kim, G.; Jeong, H. Y.; Shin, J.; Ju, Y.-W.; Han, J. W.; Kim, G. Exsolution Trends and Co-segregation Aspects of Self-grown Catalyst Nanoparticles in Perovskites. *Nat. Commun.* **2017**, *8*, 15967.
(39) Kolodiazhnyi, T.; Petric, A. The Applicability of Sr-deficient n-type $SrTiO_3$ for SOFC Anodes. *J. Electroceram.* **2005**, *15*, 5−11.
(40) Miruszewski, T.; Bochentyn, B.; Karczewski, J.; Gazda, M.; Kusz, B. Microstructural and Electrical Properties of $Y_{0.07}Sr_{0.93-x}TiO_{3-\delta}$ Perovskite Ceramics. *Cent. Eur. J. Phys.* **2012**, *10*, 1202−1209.
(41) Jansa, Z.; Prušáková, L.; Alarab, F.; Šutta, P.; Minár, J. Structural Analysis of Ni-Doped $SrTiO_3$: XRD Study. *AIP Conf. Proc.* **2019**, *2131*, 020022.

https://doi.org/10.1021/acs.energyfuels.1c01985
Energy Fuels XXXX, XXX, XXX−XXX

(42) Kamecki, B.; Miruszewski, T.; Górnicka, K.; Klimczuk, T.; Karczewski, J. Characterization Methods of Nickel Nano-particles Obtained by the Exsolution Process on the Surface of Pr, Ni-doped $SrTiO_3$ Perovskite Ceramics. *SN Appl. Sci.* **2019**, *1*, 322.
(43) Liu, J.; Wang, J.; Belotti, A.; Ciucci, F. P-Substituted $Ba_{0.95}La_{0.05}FeO_{3-\delta}$ as a Cathode Material for SOFCs. *ACS Appl. Energy Mater.* **2019**, *2*, 5472−5480.
(44) Sameshima, S.; Kawaminami, M.; Hirata, Y. Thermal Expansion of Rare-earth-doped Ceria Ceramics. *J. Ceram. Soc. Jpn.* **2002**, *110*, 597−600.
(45) Tsekouras, G.; Neagu, D.; Irvine, J. T. S. Step-change in High Temperature Steam Electrolysis Performance of Perovskite Oxide Cathodes with Exsolution of B-site Dopants. *Energy Environ. Sci.* **2013**, *6*, 256−266.
(46) Moulder, J. F.; Stickle, W. F.; Sobol, P. E.; Bomben, K. D. *Handbook of X-Ray Photoelectron Spectroscopy: A Reference Book of Standard Spectra for Identification and Interpretation of XPS data-Physical Electronics*; PerkinElmer, Inc.: United States, 1995.
(47) Naumkin, A. V.; Kraut-Vass, A.; Gaarenstroom, S. W.; Powell, C. J.. *NIST X-ray Photoelectron Spectroscopy Database, NIST Standard Reference Database 20*, Version 4.1, 2017. http://dx.doi.org/10.18434/T4T88K (accessed 2021 03 10).
(48) Emery, A. A.; Wolverton, C. High-Throughput DFT calculations of Formation Energy, Stability and Oxygen Vacancy Formation Energy of ABO_3 Perovskites. *Sci. Data* **2017**, *4*, 170153.
(49) Dabrowski, B.; Chmaissem, O.; Klamut, P. W.; Kolesnik, S.; Maxwell, M.; Mais, J.; Ito, Y.; Armstrong, B. D.; Jorgensen, J. D.; Short, S. Reduced Ferromagnetic Transition Temperatures in $SrRu_{1-v}O_3$ perovskites from Ru-site vacancies. *Phys. Rev. B: Condens. Matter Mater. Phys.* **2004**, *70*, 014423.
(50) Brakkee, R.; Williams, R. M. Minimizing Defect States in Lead Halide Perovskite Solar Cell Materials. *Appl. Sci.* **2020**, *10*, 3061.
(51) Brown, I. D.; Shannon, R. D. Empirical Bond-strength−bond-length Curves for Oxides. *Acta Crystallogr., Sect. A: Found. Adv.* **1973**, *29*, 266−282.
(52) Shahid, M.; Tiwari, P.; Basu, S. Performance Comparison of Ni Ex-soluted and Impregnated La- and Y- doped Sr Titanates as Anode for Solid Oxide Fuel Cell. *Ionics* **2019**, *25*, 171−180.
(53) Okada, K.; Kameshima, Y.; Yasumori, A. Chemical Shifts of Silicon X-ray Photoelectron Spectra by Polymerization Structures of Silicates. *J. Am. Ceram. Soc.* **1998**, *81*, 1970−1972.
(54) Furlan, A.; Gueorguiev, G. K.; Czigány, Z.; Darakchieva, V.; Braun, S.; Correia, M. R.; Högberg, H.; Hultman, L. Structure and Properties of Phosphorus-carbide Thin Solid Films. *Thin Solid Films* **2013**, *548*, 247−254.
(55) Ciucci, F.; Chen, C. Analysis of Electrochemical Impedance Spectroscopy data using the Distribution of Relaxation Times: A Bayesian and Hierarchical Bayesian Approach. *Electrochim. Acta* **2015**, *167*, 439−454.
(56) Effat, M. B.; Ciucci, F. Bayesian and Hierarchical Bayesian Based Regularization for Deconvolving the Distribution of Relaxation Times from Electrochemical Impedance Spectroscopy Data. *Electrochim. Acta* **2017**, *247*, 1117−1129.
(57) Wan, T. H.; Saccoccio, M.; Chen, C.; Ciucci, F. Influence of the Discretization Methods on the Distribution of Relaxation Times Deconvolution: Implementing Radial Basis Functions with DRTtools. *Electrochim. Acta* **2015**, *184*, 483.
(58) Escudero, M. J.; Aguadero, A.; Alonso, J. A.; Daza, L. A Kinetic Study of Oxygen Reduction Reaction on La_2NiO_4 Cathodes by means of Impedance Spectroscopy. *J. Electroanal. Chem.* **2007**, *611*, 107−116.
(59) O'hayre, R.; Cha, S.-W.; Colella, W.; Prinz, F. B. *Fuel Cell Fundamentals*, 3rd ed.; Wiley, 2016..
(60) Nielsen, J.; Hjelm, J. Impedance of SOFC Electrodes: A Review and a Comprehensive Case Study on the Impedance of LSM:YSZ Cathodes. *Electrochim. Acta* **2014**, *115*, 31−45.

https://doi.org/10.1021/acs.energyfuels.1c01985
Energy Fuels XXXX, XXX, XXX−XXX